



Carbon Coated α -Fe₂O₃ Photoanode Synthesized by a Facile Anodic Electrodeposition for Highly Efficient Water Oxidation

Honglei Zhang¹ · Longzhu Li^{2,3} · Changhai Liu² · Wenchang Wang¹ · Penghua Liang¹ · Naotoshi Mitsuzak⁴ · Zhidong Chen¹

Received: 29 August 2017 / Accepted: 29 December 2017 / Published online: 3 March 2018
© The Korean Institute of Metals and Materials 2018

Abstract

This work provides a facile anodic electrodeposition method for synthesizing carbon coated α -Fe₂O₃ photoanode followed by annealing treatment with argon atmosphere. Compared with bare hematite photoanode, the carbon coated α -Fe₂O₃ photoanodes annealed at lower temperature (Fe₂O₃/C-L) and higher temperature (Fe₂O₃/C-H) have higher photocurrent density as 0.3 and 0.5 mA cm⁻² (at 1.23 V vs. RHE), respectively. The excellent PEC performance is attributed to the synergistic reaction of carbon and vacancy oxygen. The morphology and properties of the sample were characterized with scanning electron microscopy, transmission electron microscopy, Fourier transform infrared spectroscopy, UV–Vis spectra, X-ray diffractometry, X-ray photoelectron spectra, and photoelectrical measurements.

Keywords Water oxidation · Carbon coated α -Fe₂O₃ · Anodic electrodeposition

1 Introduction

In response to environmental problems caused by the rocketing energy needs, fabricating clean and renewable fuels become increasingly essential [1–5]. Among a range of possible fuel candidates, hydrogen is one of the most promises attributing to its environmental benign with zero carbon footprint and high energy density [6, 7]. In this regard, producing hydrogen from water by photoelectrochemical (PEC) devices harvesting sunlight has received increasing

attention, which enables recyclable use of hydrogen fuel in a green and sustainable way [8–11].

A typical PEC device consists of a highly photoactive and durable photoanode for water oxidation reactions, and it is crucial to find suitable, efficient and stable materials as photoanode. Metal oxides are superior candidates for photoanode owing to its favourable stability. For example, zinc oxide [12], bismuth vanadate [13], titanium dioxide [14], iron oxide [15] and so on. Among the various metal oxide semiconductors, hematite (α -Fe₂O₃), as a promising photoanode, is nontoxic, low-cost, abundant on the earth, and highly stable under most of the aqueous environment. In addition, with a narrower bandgap of about 2.1 eV [16], hematite can utilize approximately 40% of the solar spectrum, and its theoretical solar-to-hydrogen (STH) efficiency up to 12.9% [17]. However, low conductivity, rapid electron–hole recombination rate, short carrier diffusion length (2–4 nm) and sluggish oxygen-evolution kinetic are intrinsic limitations of hematite for effective solar water splitting [18]. Various avoidance approaches have been proposed to resolve these limitations, including element doping, nanostructure engineering, and surface modifications [19, 20].

Hematite photoanode can be synthesized by plenty of methods such as colloidal method [21], hydrothermal method [22], spray pyrolysis method [23], atomic layer deposition method [24]. Compared to other synthesis

Electronic supplementary material The online version of this article (<https://doi.org/10.1007/s13391-018-0036-z>) contains supplementary material, which is available to authorized users.

✉ Zhidong Chen
zdchen@cczu.edu.cn

¹ School of Petrochemical Engineering, Changzhou University, Changzhou 213164, Jiangsu, China

² School of Materials Science and Engineering, Changzhou University, Changzhou 213164, Jiangsu, China

³ Department of Chemical and Materials Engineering, Changzhou Vocational Institute of Engineering, Changzhou 213164, Jiangsu, China

⁴ Qualtec Co., Ltd, Osaka 590-0906, Japan

methods, the electrodeposition is a bright and alternative method because of its simplicity of operation, ambient temperature and pressure processing conditions and the ability to control the crystallinity, phase composition as well as other physicochemical properties [25].

Based on previous studies, it is feasible to coat carbon layer on photoanode in order to enhance properties such as high electrical conductivity and chemical stability. Zhu et al. [26] reported that surface hybridization of TiO_2 with graphite-like carbon layers of a few molecular layers thickness yields efficient photocatalyst. Hou et al. [27] encapsulated p–n heterojunction of Cu_2O – TaON photoanode in an ultrathin graphitic carbon sheath with protecting from electrolyte to achieve enhanced PEC water oxidation performance. However, to our knowledge, no previous work has been reported regarding the application of carbon-coating $\alpha\text{-Fe}_2\text{O}_3$ photoanode by a simple and facile anodic electrodeposition in the presence of EG, as the origin of carbon.

In this paper, the EG coated FeOOH thin films were fabricated by anodic electrodeposition with additive of ethylene glycol (EG), which induced one dimensional growth just as reported by Fu et al. [28]. Furthermore, annealing the fabricated EG coated FeOOH films in argon atmosphere, the carbon coated hematite films were obtained and the EG was the carbon source.

2 Experimental

2.1 Synthesis of $\alpha\text{-Fe}_2\text{O}_3$ Photoanode

The $\alpha\text{-Fe}_2\text{O}_3$ films were prepared by anodic electrodeposition onto fluorine-doped tin oxide glass (FTO). Initially, the FTO was cleaned in an ultrasonic bath with detergent, deionized water, acetone, and ethanol for 20 min in sequence, and then dried with nitrogen gas flow. Secondly, the 25 mL aqueous electrodeposition solution consisted of 0.1 M $\text{FeCl}_2\cdot 4\text{H}_2\text{O}$ and ethylene glycol was prepared, in which the volume ratio of EG to H_2O is 1/8. Iron oxide (FeOOH) was deposited onto FTO at 70 °C and 1.2 V in a three-electrode equipment with FTO as the working electrode, the graphite rod as the counter electrode, and Ag/AgCl electrode as the reference electrode. Subsequently, the resulting samples were thoroughly rinsed with deionized water and annealed to transfer to $\alpha\text{-Fe}_2\text{O}_3$ with four different annealing regimes. Specifically, the samples annealed with lower temperature of 500 °C for 2 h in air atmosphere were denoted as $\text{Fe}_2\text{O}_3\text{-L}$ and in argon atmosphere as $\text{Fe}_2\text{O}_3\text{/C-L}$. The samples annealed with 750 °C for a short time after low temperature treatment in air atmosphere denoted as $\text{Fe}_2\text{O}_3\text{-H}$ and in argon atmosphere as $\text{Fe}_2\text{O}_3\text{/C-H}$.

2.2 Structural Characterization

The structure of iron oxide films was characterized by X-ray diffraction patterns (max 2500 PC) with $\text{CuK}\alpha$ radiation ($\lambda=0.154059$ nm) at 40 kV and 150 mA. The UV–Vis absorption spectroscopy (Shimadzu, UV 2450) was used to explore the optical properties. Surface morphology and microstructure was characterized by scanning electron microscopy (SEM, JEOL, JSM-6360LA, 20 kV) and transmission electron microscopy (TEM, JEOL, JEM-2100). And the surface functional groups were determined by Fourier transform infrared spectroscopy (FTIR, Nicolet IN10, Thermo Scientific). The element compositions of samples were determined by X-ray photoelectron spectroscopy (XPS, ESCALab 250Xi, Thermo Scientific).

2.3 Photoelectrochemical Measurement

Photoelectrochemical measurement was carried out using a standard three-electrode electrochemical workstation (LK5600), in which the fabricated samples as working electrode, a platinum foil as the counter electrode and an Ag/AgCl (sat. KCl, $E=0.1976$ V vs. RHE.) as the reference electrode. The 1 M NaOH ($\text{pH}=13.6$) was used as electrolyte, and the simulated solar light irradiation was AM 1.5 global and 1 sun (100 mW cm^{-2}). Photocurrent was measured by linear sweep voltammetry from 0.4 to 1.7 V (vs. RHE) with a scan rate of 0.03 V s^{-1} . The Mott–Schottky (MS), open circuit potential (OCP) and electrochemical impedance spectroscopy (EIS) were measured by VersaSTAT 3 potentiostat. The MS plots were measured in the dark at 1 kHz, the OCP transient tested was carried out under chopped light, and the EIS measurements were performed at OCP with the frequency range being adjusted between 100 kHz to 0.1 Hz at amplitude frequency 10 mV under light irradiation.

3 Results and Discussion

As seen in Fig. 1 and Fig. S1, the fabricated samples have the similar morphology as nanoparticle under different annealing regime. The thickness of the films is around 200 nm and the average size of the nanoparticles increases from 20–30 to 50–60 nm with higher annealing temperature. Just as previously reported [29], the higher temperature accelerates the migration of surface atoms, which helps the incorporation of iron and oxygen atoms into the lattice sites, and thus the grains size increase.

As shown in Fig. 2a, compared with the well crystalline FeOOH characteristic peaks (JCPDS No: 75-1594),

Fig. 1 Top-view SEM images of the α - Fe_2O_3 photoanode. **a** Fe_2O_3 -L, **b** Fe_2O_3 -H, **c** Fe_2O_3 /C-L, **d** Fe_2O_3 /C-H

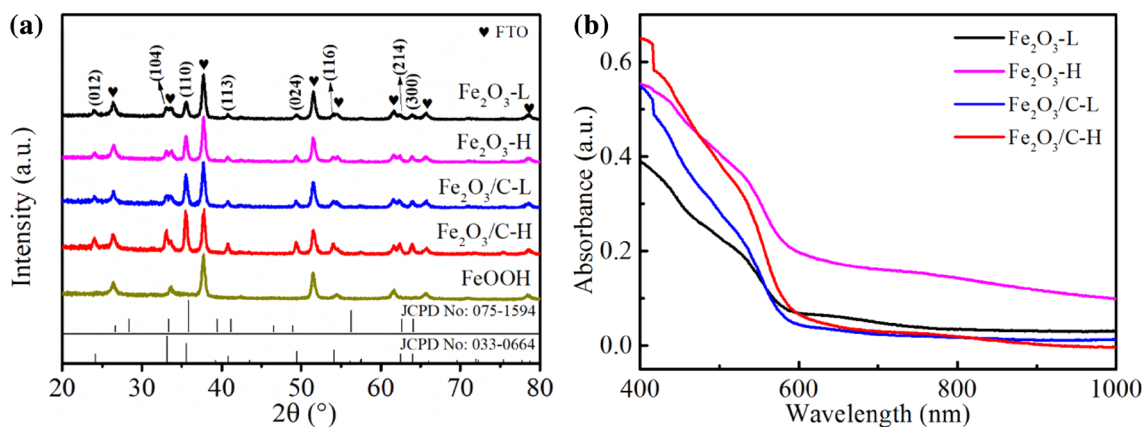
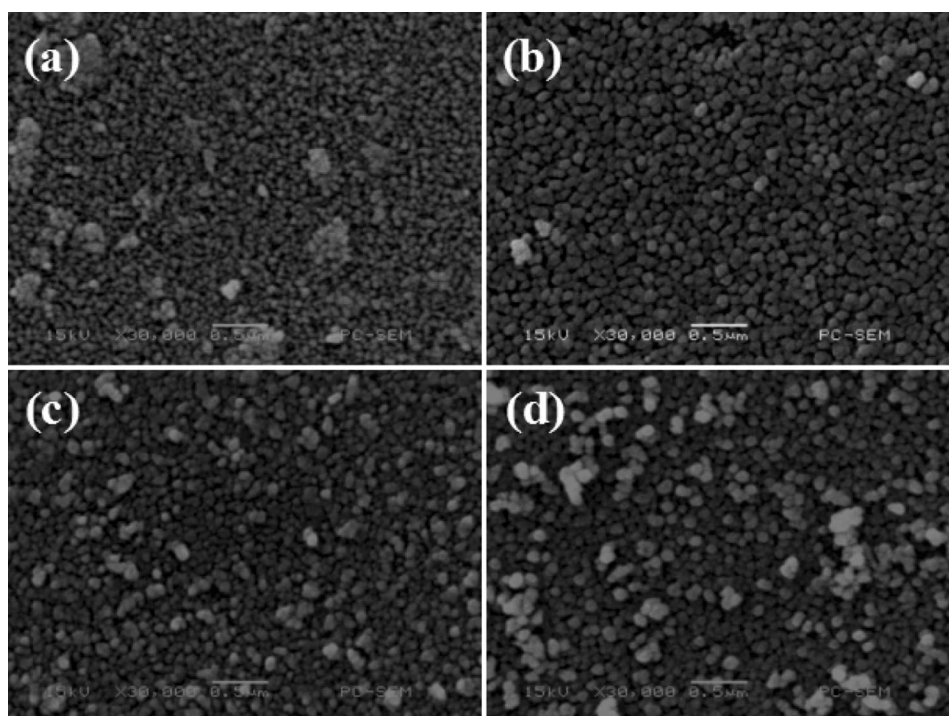


Fig. 2 **a** X-Ray diffraction patterns and **b** UV–Vis absorbance spectra of the samples

amorphous FeOOH film formed during the electrodeposition process has no corresponding peak signal in XRD pattern. While annealed at four different conditions, films became crystalline, giving strong diffraction peaks matching to the characteristic peaks of α - Fe_2O_3 (JCPDS No: 33-0664). No peak intensity of FeOOH is found in all of the fabricated α - Fe_2O_3 films compared with the characteristic peaks of FeOOH , which indicate that FeOOH is completely transformed into α - Fe_2O_3 after heat treatment process. All of the fabricated α - Fe_2O_3 films demonstrate the obvious diffraction peak of (110), which indicates preferential growth along [110] direction and improves hematite's conductivity [28]. The relative peak intensity of

the samples shows no distinct difference, but the intensity of [110] orientation is enhanced and the half-peak width decreased under higher temperature annealing. As shown in Fig. S2, the half-peak width of Fe_2O_3 -L and Fe_2O_3 -H electrodes are 0.429 and 0.363 respectively, while they are 0.382 and 0.356 for Fe_2O_3 /C-L and Fe_2O_3 /C-H electrodes respectively. It is reported that the crystallinity of the electrode will be enhanced as the annealing temperature rise, which could be conducive to improve hematite's PEC performance [30]. The UV–Vis absorbance spectra of the fabricated photoanodes (Fig. 2b) have a clear absorption edge around 600 nm, corresponding to the band gap energy of the typical hematite electrodes of 2.1–2.2 eV.

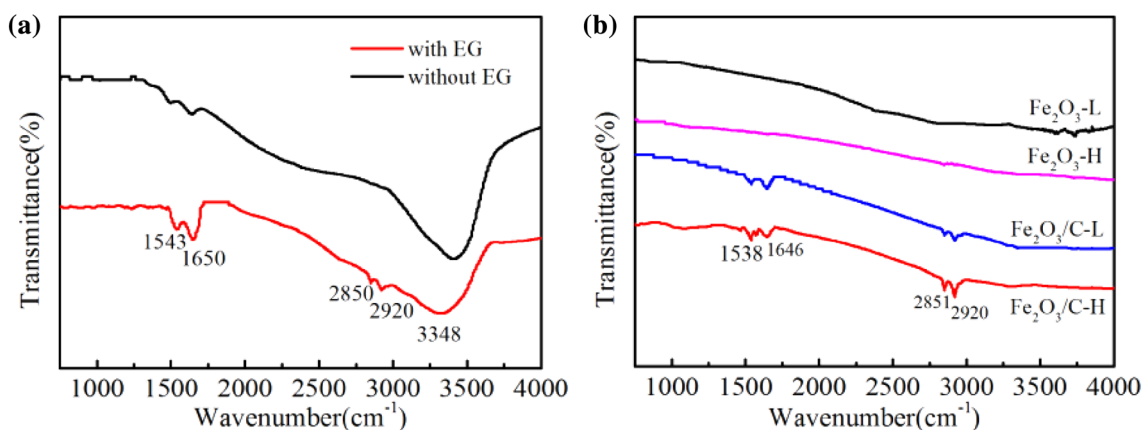


Fig. 3 Fourier transform infrared spectroscopy of as-deposited (a) and annealed (b) films

FTIR spectrum is used to determine the surface functional groups of the fabricated electrodes. From Fig. 3a, the as-deposited electrode deposited with EG shows two distinct peaks at 2850 and 2920 cm^{-1} , which can be assigned to symmetric and asymmetric stretching vibration of the $-\text{CH}_2$ bond. It can be confirmed that the amorphous lepidocrocite is coated with the short carbon chain of EG. Besides, the FTIR peak at 3348 cm^{-1} corresponds to the stretching vibration of $-\text{OH}$. The peaks at 1543 and 1650 cm^{-1} are ascribed to $\text{C}=\text{C}$ stretching vibration, which can also be observed when the film was deposited without EG. However, these two peaks disappear when Pt used as counter electrode (seen in Fig. S3). It can be concluded that the $\text{C}=\text{C}$ peaks are caused by some quantity of carbon adsorbed in the photoelectrode in the process of deposition for the graphite rod used as counter electrode. As seen from Fig. 3b, after annealing at four different annealing regimes, the peak of $-\text{OH}$ disappears with FeOOH converting to $\alpha\text{-Fe}_2\text{O}_3$, which are in consonance with the results of XRD. While, the carbon peaks of fabricated electrodes $\text{Fe}_2\text{O}_3\text{-L}$ and $\text{Fe}_2\text{O}_3\text{-H}$ annealed in air atmosphere disappear due to the burning of EG to form carbon dioxide. Contrarily, annealed in argon atmosphere, the carbon peaks of $\text{Fe}_2\text{O}_3\text{/C-L}$ and $\text{Fe}_2\text{O}_3\text{/C-H}$ electrode observed still. It demonstrates that carbon-coated hematite photoanode obtained under argon atmosphere annealing. To further ascertain the existence of carbon on the electrode, TEM measurement was carried out. Fig. S4 shows the HRTEM images of $\text{Fe}_2\text{O}_3\text{/C}$ samples. It clearly reveals the lattice fringe with 0.257 nm which correspond to (110) plane of $\alpha\text{-Fe}_2\text{O}_3$. A thin and nonuniform carbon layer with average thickness of less than 1.5 nm was observed on the surface of $\alpha\text{-Fe}_2\text{O}_3$.

In order to confirm the surface composition of the $\text{Fe}_2\text{O}_3\text{/C-L}$ and $\text{Fe}_2\text{O}_3\text{/C-H}$ electrodes, X-ray photoelectron spectroscopy (XPS) was carried out and the results are shown in Fig. 4. The full-scale XPS spectra (Fig. 4a)

reveal the presence of Fe, O and C elements in $\text{Fe}_2\text{O}_3\text{/C-L}$ and $\text{Fe}_2\text{O}_3\text{/C-H}$ electrodes. The Fe and O signals are from $\alpha\text{-Fe}_2\text{O}_3$. The C peak is attributed to EG in accordance with the result of FTIR, which demonstrates the carbon is retained in Argon atmosphere annealing condition. As shown in higher resolution curves of Fe 2p (Fig. 4b), the two peaks located at 710.7 and 723.8 eV can be assigned to the signals of Fe 2p_{3/2} and Fe 2p_{1/2} corresponding to the typical trivalent Fe species. For two electrodes, there is a small peak at lower binding energy of Fe 2p_{3/2} corresponding to the divalent Fe. Yan et al. [31] indicates the existence of Fe^{2+} in the hematite lattice was achieved by annealing in a lack of oxygen atmosphere, e.g. in Argon. As shown in Fig. 4c, d, for $\text{Fe}_2\text{O}_3\text{/C-L}$ and $\text{Fe}_2\text{O}_3\text{/C-H}$ electrodes, the observed main peak at 529.9 eV (O 1s) is due to oxygen atoms bound to metals, while the shoulder peak at higher binding energy is attributed to the defect sites with a low oxygen coordination, i.e. oxygen vacancies [32, 33]. Deconvolution of the O 1s spectra shows that the intensity of the shoulder peak around 532 eV relative to that of the main oxide peak at 529.9 eV increases from 0.56 to 3.30 for the $\text{Fe}_2\text{O}_3\text{/C-L}$ and $\text{Fe}_2\text{O}_3\text{/C-H}$ electrodes respectively. Obviously, for $\text{Fe}_2\text{O}_3\text{/C-H}$ electrode, the density of oxygen vacancies is much higher than the $\text{Fe}_2\text{O}_3\text{/C-L}$ electrode, and it can be concluded that the higher temperature can increase the density of oxygen vacancies.

To investigate the PEC performance of the as-prepared photoanodes with four different annealing regimes, the photocurrent response under simulated solar light irradiation has been measured shown in Fig. 5a. It is observed that the sample $\text{Fe}_2\text{O}_3\text{-L}$ yielded very low photocurrent density, indicating that carrier generation and their separation were limited due to the poor charge transport properties of crystalline hematite. $\text{Fe}_2\text{O}_3\text{-H}$ photoanode shows enhanced photocurrent density for the effect of improved crystallinity and additional charge carriers in hematite nanoparticles, which

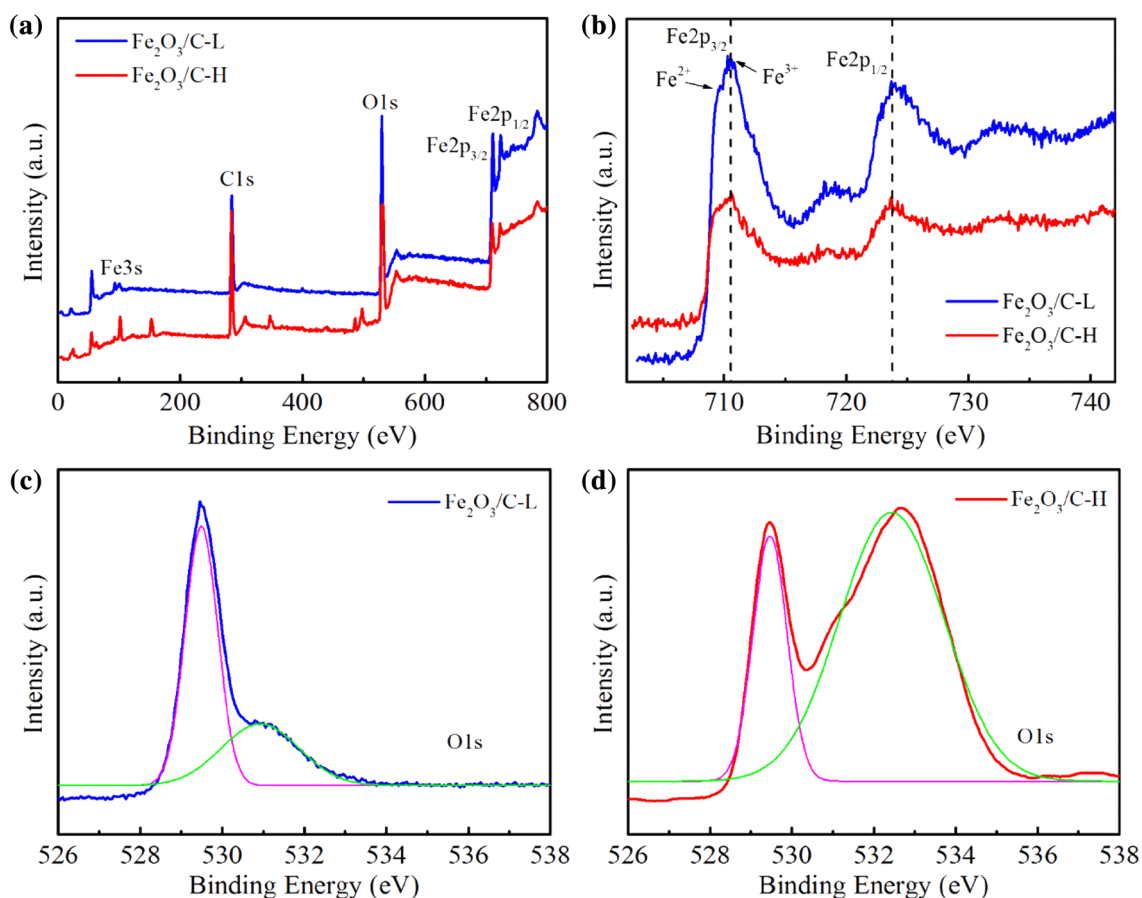


Fig. 4 a XPS survey spectrum, high resolution, b Fe 2p and c, d O 1s XPS spectra collected for Fe₂O₃/C-L and Fe₂O₃/C-H electrodes

caused by the doping of Sn⁴⁺ ions diffused from FTO with higher temperature annealing [34]. The fabricated photoanode Fe₂O₃/C-L and Fe₂O₃/C-H annealed in argon atmosphere show improved photocurrent density as 0.3 mA cm² and 0.5 mA cm² at 1.23 V (vs. RHE), respectively. The main reason may be attributed to the coated carbon and vacancy oxygen. Hou et al. [27] indicated that the carbon layer can behave as an electron conductor to enhance the electron–hole separation and easily transfer electrons. Freitas et al. [35] indicated that inert gas annealing enhance the catalytic efficiency of α -Fe₂O₃ surface by effectively increasing the rate of hole transfer to the electrolyte. In order to prove the effect of carbon caused by EG, the photocurrent response of the electrode deposited with and without EG annealed at higher temperature and argon atmosphere is shown in Fig. S5. It can be concluded that the carbon can enhanced the photocurrent response of the photoelectrode. As shown in Fig. 5b, the photocurrent response measurements were performed under back-side and front-side illuminations for all samples. The photoanodes annealed in air atmosphere have higher photocurrent density under back-side illumination than front-side, which is in agreement with the literature

[36]. For front-side illumination, electrons have to travel a longer distance to FTO compared to back-side illumination where the accumulation of charge is higher. On the contrary, the photoanodes annealed in argon atmosphere have higher photocurrent density under front-side illumination. It can be attributed to the increased electron conductivity caused by coated-carbon and vacancy oxygen in the surface of hematite. The holes generated near the semiconductor-electrolyte interface injected easily into the electrolyte and electrons are easier to traverse to the back contact, implying higher photocurrent density under front side illumination. The stability tests shown in Fig. 5c, all the fabricated samples show a good stability during measuring time.

To clarify the origin of the different photocurrent response and electron transport mechanism of the fabricated electrode, Mott–Schottky (MS) analysis was performed and the results are shown in Fig. S6. The positive slopes of MS plots indicate that all of the electrodes are n-type semiconductor with electrons as the majority carriers. Although the MS analysis is derived from a planar electrode model, it is still reasonable to calculate the carrier density for comparison purpose [37]. The carrier densities calculated from

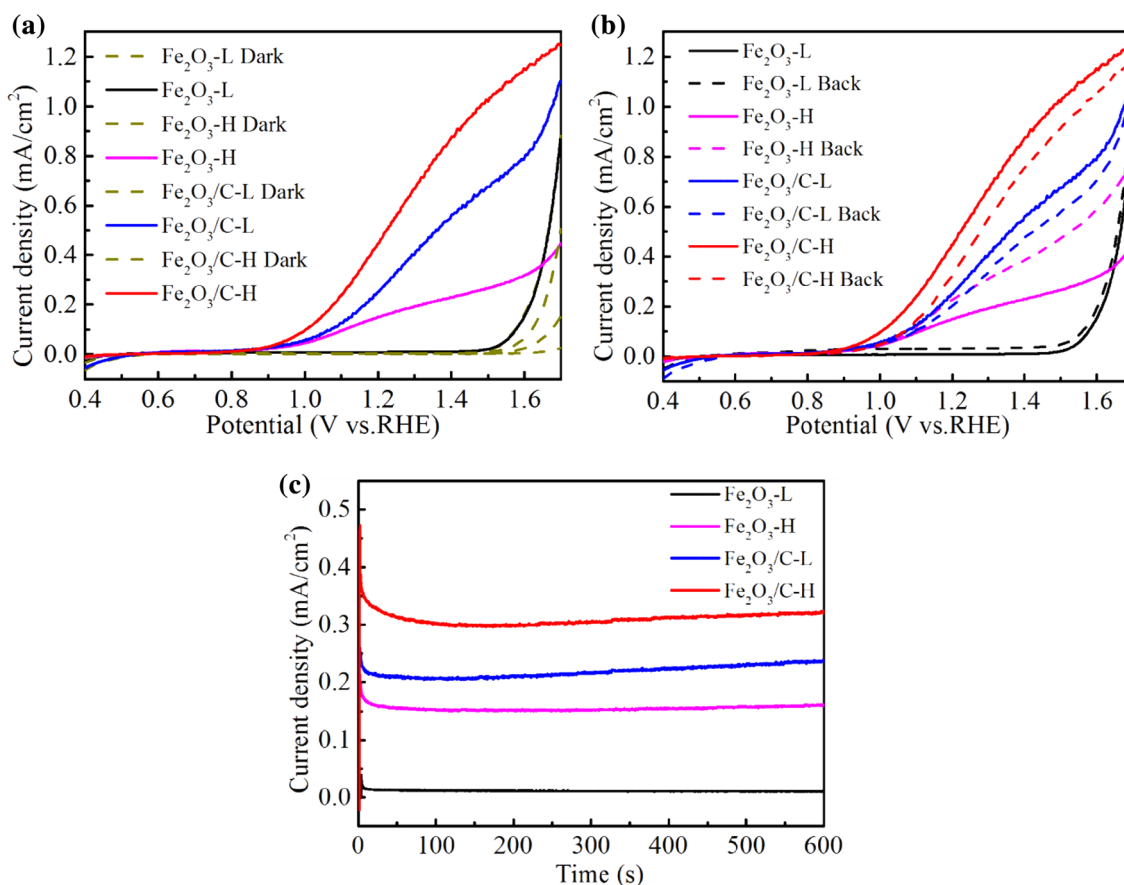


Fig. 5 Photocurrent densities-potential curves of the fabricated photoanodes [AM 1.5 global, 1 sun (100 mW cm^{-2})]. **a** Front side-illuminated and dark, **b** front- and back-side illumination. **c** Stability of fabricated photoanodes under light illumination at 1.23 V (vs. RHE)

the slopes of the MS plots for $\text{Fe}_2\text{O}_3\text{-L}$ and $\text{Fe}_2\text{O}_3\text{/C-L}$ are 3.28×10^{24} and $6.28 \times 10^{25} \text{ m}^{-3}$, respectively. The difference was likely to be generated by the increased electron conductivity caused by coated-carbon and vacancy oxygen. Similarly, for $\text{Fe}_2\text{O}_3\text{/C-H}$ electrodes, the carrier density is $2.15 \times 10^{25} \text{ m}^{-3}$, about four times more than the value of $5.80 \times 10^{24} \text{ m}^{-3}$ for $\text{Fe}_2\text{O}_3\text{-H}$ electrode.

To further probe the quality of the photoanode/electrolyte junction, the open circuit potential (OCP) transient tests of the prepared samples are carried out and the results are shown in Fig. 6. It was noted that the generated photovoltage (equal to the difference of open circuit voltage upon light illumination and in dark) of the $\text{Fe}_2\text{O}_3\text{/C-H}$ and $\text{Fe}_2\text{O}_3\text{/C-L}$ samples (0.209 and 0.184 V vs. Ag/AgCl) are larger than that of the $\text{Fe}_2\text{O}_3\text{-H}$ and $\text{Fe}_2\text{O}_3\text{-L}$ samples (0.182 and 0.166 V vs. Ag/AgCl) as the light was on, indicating that the prepared samples annealed in argon atmosphere show more remarkable photoelectric conversion ability.

To explore the charge dynamics of the photoanodes, EIS is performed for all the samples under front side illumination as Fig. 7. The Nyquist impedance of the fabricated photoanodes analyzed in a frequency range of 0.1– 10^5 Hz

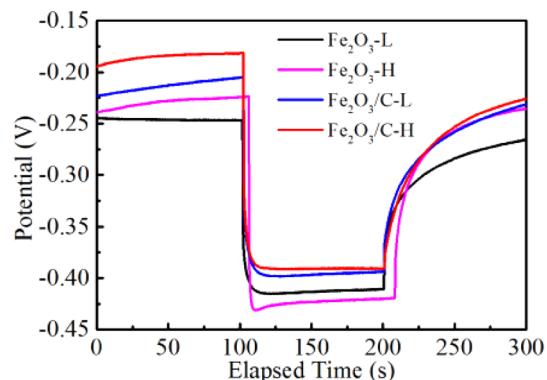


Fig. 6 Open circuit potential (OCP) curves of the fabricated photoanodes under chopped light

and the corresponding equivalent circuit model fitted from the obtained EIS data by program Zsimpwin, in which the dots in the plots represent the experimental data and the solid lines represent the result of fitting. The EIS equivalent circuit model includes two sub-circuit which containing a resistance and a capacitance (RC) in parallel circuits.

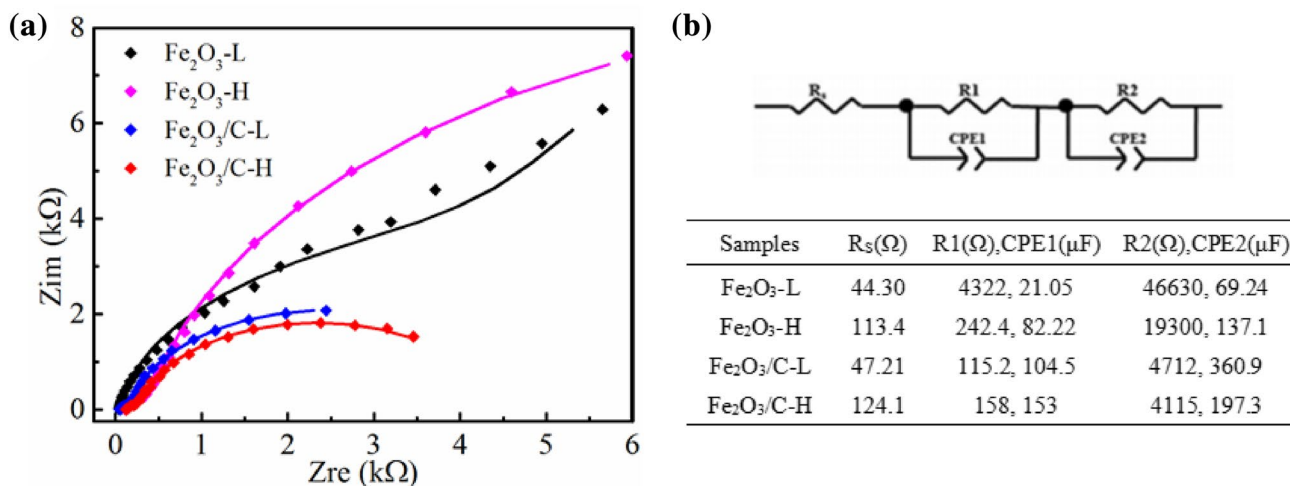


Fig. 7 **a** Nyquist plots of the fabricated photoanodes. **b** Corresponding equivalent circuit model and fitting impedance parameter values

The fitted impedance parameter values of the resistances (R) and constant phase elements (CPE) are listed in Fig. 7b. The small semicircle at high frequency ($R1/CPE1$) reflected the recombination of charges in bulk. The large semicircle at low-frequency ($R2/CPE2$) represent the larger interface resistance between n-type semiconductor electrode and electrolyte, which is the most difficult process of an entire photoelectrochemical reaction system [38–40]. Comparing the sample $Fe_2O_3/C-H$ to Fe_2O_3-H , and $Fe_2O_3/C-L$ to Fe_2O_3-L , the fitting results indicated that the photoanodes annealed with argon atmosphere exhibit lower resistance $R1$ for electrons recombining with holes and the charge transfer resistance $R2$ from the surface state of the electrode. The Fe_2O_3/C photoanodes with lower resistance $R1$ indicates decreased electron–hole recombination attributed to the excellent electrical nature of coated-carbon and vacancy oxygen. The Fe_2O_3-H photoanode exhibit lower resistance $R1$ comparing to Fe_2O_3-L , the main reason is that the reduced grain boundaries and Sn-doping in proximity to the FTO interface coincide with the result of Glasscock [41]. While the $Fe_2O_3/C-H$ photoanode exhibit higher resistance $R1$ comparing to $Fe_2O_3/C-L$ attributed to the coated-carbon reducing with higher annealing temperature according to the result of FTIR and XPS, which indirectly indicate the coated-carbon is the main imaging factor of bulk recombination. Furthermore, the small value of $R2$ of Fe_2O_3/C photoanodes results in faster hole transfer at the surface, which relates to the vacancy oxygen to the fast OCP-decay behavior in Fig. S7.

To further account for the bulk and surface charge transfer efficiency for the above samples, photocurrent response in the presence of a hole scavenger with 0.5 M H_2O_2 in the 1 M NaOH electrolyte was performed as shown in Fig. 8a. According to the report of Dotan [42], the addition of H_2O_2 to the electrolyte removes the injection barrier but does not

affect charge separation within the space charge layer of the hematite electrodes. And the surface charge injection ($\eta_{surface}$) and bulk charge separation efficiencies (η_{bulk}) for these samples in the voltage region occurring before their dark current onset were calculated in detail in Section S6, and the results are shown in Fig. 8b, c. It can be seen that the $\eta_{surface}$ of $Fe_2O_3/C-H$ is close to zero up to the photocurrent onset potential (0.85 V vs. RHE) and then it rises steeply up to 90% at high potentials resulted from deactivation of surface traps at the electrode/electrolyte interface. The $Fe_2O_3/C-H$ photoanode has higher $\eta_{surface}$ than the others for the vacancy oxygen, which confirmed the result of EIS. As seen in Fig. 8c, the difference of η_{bulk} of the $Fe_2O_3/C-L$ and Fe_2O_3-L is larger than $Fe_2O_3/C-H$ and Fe_2O_3-H photoanode attributed to the coated-carbon which increased the electron conductivity of photoanode. It can be concluded that the synergistic reaction of carbon and vacancy oxygen caused the excellent PEC performance of the Fe_2O_3/C photoanode.

4 Conclusions

In this study, anodic electrodeposition method was used for synthesizing carbon coated $\alpha-Fe_2O_3$ photoanode followed by annealing treatment with argon atmosphere. After annealing at four different annealing regimes, the $Fe_2O_3/C-L$ and $Fe_2O_3/C-H$ photoanodes have higher photocurrent density as 0.3 and 0.5 mA cm⁻² (at 1.23 V vs. RHE), respectively. FTIR, HRTEM and XPS analysis verify that the carbon element indeed exists in the $\alpha-Fe_2O_3$ photoanode before and after annealing treatment with argon atmosphere. Furthermore, O 1s spectra demonstrate that the number of oxygen vacancies increase at higher temperature. The coated carbon and vacancy oxygen increased electron conductivity, which is crucial for

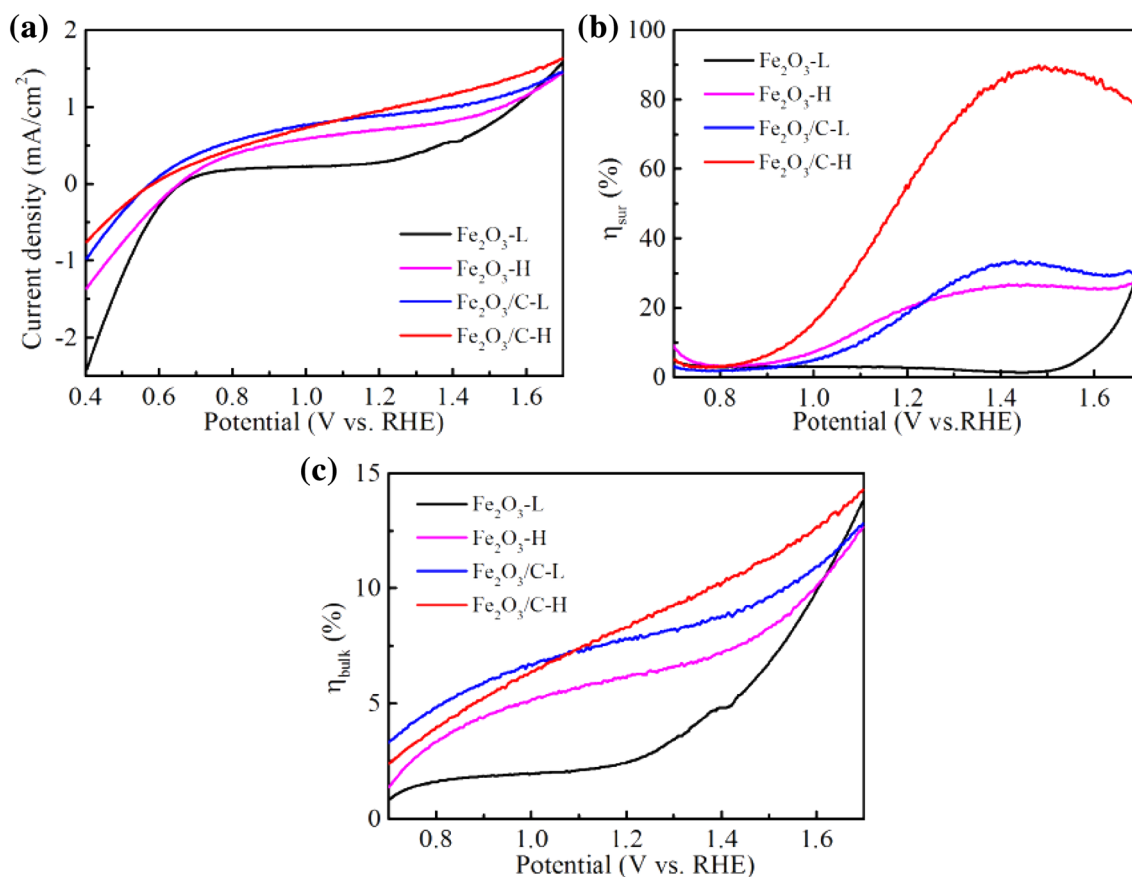


Fig. 8 a Photocurrent densities-potential curves of the fabricated photoanodes measured in 1.0 M NaOH and 0.5 M H₂O₂ under illumination, b Charge separation efficiency on the surface (η_{surface}) and c in the bulk (η_{bulk}) of the fabricated photoanodes

promoting the charge separation efficiency in the bulk. And the faster hole transfer at the surface was attributed to the vacancy oxygen, which is crucial for promoting the charge separation efficiency in the surface. The excellent PEC performance was attributed to the synergistic reaction of carbon and vacancy oxygen, which was demonstrated by the Mott–Schottky, EIS analysis and the I–V characterization, as well as the I–V characteristics with H₂O₂ as the hole scavenger. Future work will focus on the improvement of the hematite structure and further surface modification aiming at less charge recombination and better photoelectrochemical performance.

Acknowledgements This work was supported by the National Natural Science Foundation of China (Nos. 51702025, 51574047), Natural Science Foundation of Jiangsu Province (No. BK20160277), Natural Science Foundation of the Jiangsu Higher Education Institutions of China (Grant No. 16KJA430004).

References

- Fujishima, A., Honda, K.: Electrochemical photolysis of water at a semiconductor electrode. *Nature* **238**, 37 (1972)
- Lewis, N.S., Nocera, D.G.: Powering the planet: chemical challenges in solar energy utilization. *Proc. Natl. Acad. Sci. USA* **103**, 15729 (2006)
- Grätzel, M.: Photoelectrochemical cells. *Nature* **414**, 338 (2001)
- Walter, M.G., Warren, E.L., McKone, J.R., Boettcher, S.W., Mi, Q., Santori, E.A., Lewis, N.S.: Solar water splitting cells. *Chem. Rev.* **110**, 6446 (2010)
- Chatzitakis, A., Nikolakaki, E., Sotiropoulos, S., Poullos, I.: Hydrogen production using a photoelectrocatalytic-enzymatic hybrid system. *Catal. Today* **209**, 60 (2013)
- Park, H., Vecitis, C.D., Hoffmann, M.R.: Solar-powered electrochemical oxidation of organic compounds coupled with the cathodic production of molecular hydrogen. *J. Phys. Chem. A* **112**, 7616 (2008)
- Park, H., Vecitis, C.D., Hoffmann, M.R.: Electrochemical water splitting coupled with organic compound oxidation: the role of active chlorine species. *J. Phys. Chem. C* **113**, 7935 (2009)
- Zhang, P., Zhang, J., Gong, J.: Tantalum-based semiconductors for solar water splitting. *Chem. Soc. Rev.* **43**, 4395 (2014)
- Qureshy, A.M., Ahmed, M., Dincer, I.: Simulation of transport phenomena in a photoelectrochemical reactor for solar hydrogen production. *Int. J. Hydrog. Energy* **41**, 8020 (2016)
- Suarez, C.M., Hernandez, S., Russo, N.: BiVO₄ as photocatalyst for solar fuels production through water splitting: a short review. *Appl. Catal. A Gen.* **504**, 158 (2015)

11. Molinari, R., Marino, T., Argurio, P.: Photocatalytic membrane reactors for hydrogen production from water. *Int. J. Hydrog. Energy* **39**, 7247 (2014)
12. Lei, Y., Zhao, G., Liu, M., Zhang, Z., Tong, X., Cao, T.: Fabrication, characterization, and photoelectrocatalytic application of ZnO nanorods grafted on vertically aligned TiO₂ nanotubes. *J. Phys. Chem. C* **113**, 19067 (2009)
13. Park, H.S., Kweon, K.E., Ye, H., Paek, E., Hwang, G.S., Bard, A.J.: Factors in the metal doping of BiVO₄ for improved photoelectrocatalytic activity as studied by scanning electrochemical microscopy and first-principles density-functional calculation. *J. Phys. Chem. C* **115**, 17870 (2011)
14. Vimonses, V., Chong, M.N., Jin, B.: Evaluation of the physical properties and photodegradation ability of titania nanocrystalline impregnated onto modified kaolin. *Microporous Mesoporous Mater.* **132**, 201 (2010)
15. Sivula, K., Formal, F.L., Grätzel, M.: Solar water splitting: progress using hematite (α -Fe₂O₃) photoelectrodes. *Chemsuschem* **4**, 432 (2011)
16. Kay, A., Cesar, I., Grätzel, M.: New benchmark for water photooxidation by nanostructured α -Fe₂O₃ Films. *J. Am. Chem. Soc.* **128**, 15714 (2006)
17. Murphy, A., Barnes, P., Randeniya, L.K., Plumb, I.C., Grey, I.E., Horne, M.D., Glasscock, J.A.: Efficiency of solar water splitting using semiconductor electrodes. *Int. J. Hydrog. Energy* **31**, 1999 (2006)
18. Formal, F.L., Pastor, E., Tilley, S.D., Mesa, C.A., Pendlebury, S.R., Gratzel, M., Durrant, J.R.: Rate law analysis of water oxidation on a hematite surface. *J. Am. Chem. Soc.* **137**, 6629 (2015)
19. Hamann, T.W.: Splitting water with rust: hematite photoelectrochemistry. *Dalton Trans.* **41**, 7830 (2012)
20. Noh, K.J., Kim, B.R., Yoon, G.J., Jung, S.C., Kang, W., Kim, S.J.: Microstructural effect on the photoelectrochemical performance of hematite-Fe₂O₃ photoanode for water splitting. *Electron. Mater. Lett.* **8**, 345 (2012)
21. Sivula, K., Zboril, R., Formal, F.L., Robert, R., Weidenkaff, A., Tucek, J., Frydrych, J., Grätzel, M.: Photoelectrochemical water splitting with mesoporous hematite prepared by a solution-based colloidal approach. *J. Am. Chem. Soc.* **132**, 7436 (2010)
22. Meng, F., Li, J., Cushing, S.K., Bright, J., Zhi, M., Rowley, J.D., et al.: Photocatalytic water oxidation by hematite/reduced graphene oxide composites. *ACS Catal.* **3**, 746 (2013)
23. Duret, A., Grätzel, M.: Visible light-induced water oxidation on mesoscopic α -Fe₂O₃ films made by ultrasonic spray pyrolysis. *J. Phys. Chem. B* **109**, 17184 (2005)
24. Formal, F.L., Tetreault, N., Cornuz, M., Moehl, T., Grätzel, M., Sivula, K.: Passivating surface states on water splitting hematite photoanodes with alumina overlayers. *Chem. Sci.* **2**, 737 (2011)
25. Schreiber, R., Llewelyn, C., Vera, F., Cury, P., Muñoz, E., Río, R., et al.: An electrochemical deposition route for obtaining α -Fe₂O₃ thin films II. EQCM study and semiconductor properties. *Electrochem. Solid-State Lett.* **10**, D95 (2007)
26. Zhang, L., Fu, H., Zhu, Y.: Graphene/TiO₂ nanocomposites: synthesis, characterization and application in hydrogen evolution from water photocatalytic splitting. *Adv. Funct. Mater.* **18**, 2180 (2008)
27. Hou, J., Yang, C., Cheng, H., Jiao, S., Takeda, O., Zhu, H.: High-performance p-Cu₂O/n-TaON heterojunction nanorod photoanodes passivated with an ultrathin carbon sheath for photoelectrochemical water splitting. *Energy Environ. Sci.* **7**, 3758 (2014)
28. Fu, L., Yu, H., Li, Y., Zhang, C., Wang, X., Shao, Z., Yi, B.: Ethylene glycol adjusted nanorod hematite film for active photoelectrochemical water splitting. *Phys. Chem. Chem. Phys.* **16**, 4284 (2014)
29. Caglar, Y., Ilican, S., Caglar, M., Yakuphanoglu, F., Wu, J., Gao, K., Lu, P., Xue, D.: Influence of heat treatment on the nanocrystalline structure of ZnO film deposited on p-Si. *J. Alloys Compd.* **481**, 885 (2009)
30. Phuan, Y.W., Chong, M.N., Zhu, T., Yong, S.T., Chan, E.S.: Effects of annealing temperature on the physicochemical, optical and photoelectrochemical properties of nanostructured hematite thin films prepared via electrodeposition method. *Mater. Res. Bull.* **69**, 71 (2014)
31. Yan, D., Liu, J., Shang, Z., Luo, H.: Ti-doped α -Fe₂O₃ nanorods with controllable morphology by carbon layer coating for enhanced photoelectrochemical water oxidation. *Dalton Trans.* **46**, 10558 (2017)
32. Lei, F., Sun, Y., Liu, K., Gao, S., Liang, L., Pan, B., Xie, Y.: Oxygen vacancies confined in ultrathin indium oxide porous sheets for promoted visible-light water splitting. *J. Am. Chem. Soc.* **136**, 6826 (2014)
33. Zhu, C., Li, C., Zheng, M., Delaunay, J.: Plasma-induced oxygen vacancies in ultrathin hematite nanoflakes promoting photoelectrochemical water oxidation. *ACS Appl. Mater. Interfaces* **7**, 22355 (2015)
34. Ling, Y., Wang, G., Wheeler, D.A., Zhang, J.Z., Li, Y.: Sn-doped hematite nanostructures for photoelectrochemical water splitting. *Nano Lett.* **11**, 2119 (2011)
35. Freitas, A.L.M., Carvalho, W.M., Souza, F.L.: Enhanced water oxidation efficiency of hematite thin films by oxygen-deficient atmosphere. *J. Mater. Res.* **30**, 3595 (2015)
36. Bassi, P.S., Xianglin, L., Fang, Y., Loo, J.S.C., Barber, J., Wong, L.H.: Understanding charge transport in non-doped pristine and surface passivated hematite (Fe₂O₃) nanorods under front and backside illumination in the context of light induced water splitting. *Phys. Chem. Chem. Phys.* **18**, 30370 (2016)
37. Cardon, F., Gomes, W.P.: On the determination of the flat-band potential of a semiconductor in contact with a metal or an electrolyte from the Mott-Schottky plot. *J. Phys. D Appl. Phys.* **11**, L63 (1978)
38. Xie, Y., Zhou, L., Lu, J.: Photoelectrochemical behavior of titania nanotube array grown on nanocrystalline titanium. *J. Mater. Sci.* **44**, 2907 (2009)
39. Kim, J.Y., Jun, H., Hong, S.J., Kim, H.G., Lee, J.S.: Charge transfer in iron oxide photoanode modified with carbon nanotubes for photoelectrochemical water oxidation: an electrochemical impedance study. *Int. J. Hydrog. Energy* **36**, 9462 (2011)
40. Bora, D.K., Braun, A., Constable, E.C.: "In rust we trust" Hematite-the prospective inorganic backbone for artificial photosynthesis. *Energy Environ. Sci.* **6**, 407 (2013)
41. Glasscock, J., Barnes, P., Plumb, I., Bendavid, A., Martin, P.: Structural, optical and electrical properties of undoped polycrystalline hematite thin films produced using filtered arc deposition. *Thin Solid Films* **516**, 1716 (2008)
42. Dotan, H., Sivula, K., Grätzel, M., Rothschild, A., Warren, S.C.: Probing the photoelectrochemical properties of hematite (α -Fe₂O₃) electrodes using hydrogen peroxide as a hole scavenger. *Energy Environ. Sci.* **4**, 958 (2011)